THE JOURNAL OF PHYSICAL CHEMISTRY C

pubs.acs.org/JPCC Article

# Molecular Dynamics Simulations of Mineral Surface Wettability by Water Versus $CO_2$: Thin Films, Contact Angles, and Capillary Pressure in a Silica Nanopore

Emily Wei-Hsin Sun* and Ian C. Bourg

Cite This: J. Phys. Chem. C 2020, 124, 25382−25395 Read Online

ACCESS | Metrics & More | Article Recommendations | Supporting Information

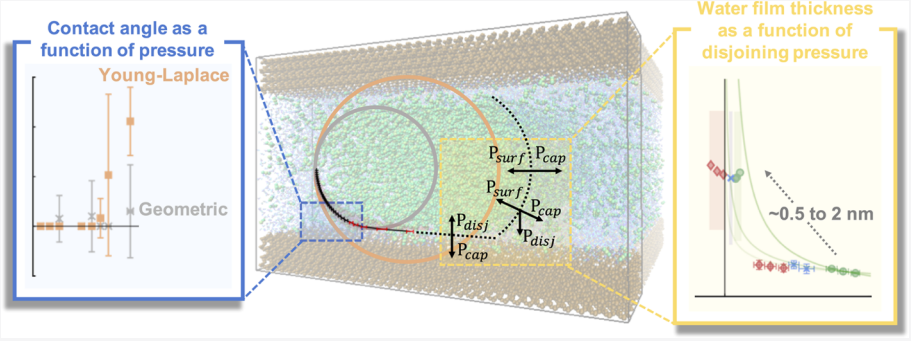


**ABSTRACT:** The wettability of mineral surfaces is an important property influencing multiphase flow in soils and sedimentary rocks. In particular, for $CO_2$ abatement technologies that rely on trapping supercritical $CO_2$ in sedimentary formations, the wettability of relevant mineral surfaces by water is a poorly constrained fundamental property influencing stratigraphic and residual trapping. Theoretical studies have noted that adsorbed water films may hold a key to resolving many of the discrepancies in reported wettability data, but the transition from the droplet to the film is difficult to observe experimentally. The link between continuum and nanoscale observations can be elucidated using molecular dynamics (MD) and thermodynamic equations. We simulate water and $CO_2$ at various pressures between quartz surfaces to probe the thickness of the adsorbed water film observed between the $CO_2$ and quartz, and the radius of curvature of the fluid−fluid interface as a function of $CO_2$ pressure. These results are discussed in the context of the relevant interfacial energies and Young's equation and the Gibbs $CO_2$ surface excesses at various interfaces. We show that the augmented Young−Laplace equation accurately captures the relationship between the observed radius of curvature, the capillary pressure between the bulk fluid phases, and the disjoining pressure in the adsorbed water film. We examine the thermodynamics of thin water films in novel depth and present a new methodology for characterizing circularity approaching a mineral interface and for comparing continuum and nanoscale manifestations of wettability. We find that discrepancies in both the experimental and MD database may be influenced by proximity to solid surfaces and adsorbed wetting films.

## 1. INTRODUCTION

Humanity's transition to a low-carbon economy over the next few decades is a defining challenge of our time with vast implications for Earth's geography, biodiversity, and climate[1] as well as for human exposure to water scarcity, extreme weather events, socio-economic inequities, and geopolitical conflicts.[2] An emerging scientific consensus is that this transition requires a combination of technologies including energy conservation, renewable energy, low-carbon energy, and negative emission technologies.[3] Among these technologies, several that rely on the ability to securely trap large plumes of supercritical $CO_2$ ($scCO_2$) in geologic formations—carbon capture and storage (CCS), bioenergy with CCS, and $CO_2$-enhanced oil recovery—have the potential to contribute substantially to $CO_2$ abatement efforts.[4−7] A crucial requirement of these technologies is the ability to predict the flow of $scCO_2$ in porous sedimentary rocks.[8,9]

The wettability of mineral surfaces by water versus $scCO_2$ is a key phenomenon that influences the flow of $scCO_2$ in porous rocks.[10−12] In particular, this wettability underlies two of the most important trapping mechanisms utilized in subsurface $CO_2$ storage: stratigraphic trapping, whereby $scCO_2$ migration into fine-grained seals and caprocks (e.g., shales) is blocked by high capillary entry pressure in water-filled nanopores,[13−15]

Received: August 31, 2020
Revised: October 14, 2020
Published: November 5, 2020






https://dx.doi.org/10.1021/acs.jpcc.0c07948
J. Phys. Chem. C 2020, 124, 25382−25395

and residual trapping, whereby multiphase flow in the storage formation (typically a sandstone) results in the fragmentation of the $scCO_2$ plume into immobile disconnected ganglia.[16,17] A fundamental parameter that determines the efficiency of both trapping mechanisms is the contact angle ($\theta$) formed by water and $scCO_2$ with mineral surfaces.[18−20]

To date, this contact angle remains poorly understood in conditions relevant to geologic carbon storage (GCS), in large part because $\theta$ values reported in different studies vary widely.[12,13,20,21] For example, $\theta$ values measured on stringently cleaned quartz surfaces range from around 0° (strongly water-wet) to nearly 55° (intermediate-wet), and trends with increasing pressure have been reported as both increasing and constant.[12,22−25] This wide range of observations, unfortunately, makes it difficult to confidently predict multiphase flow patterns in sedimentary rocks.[17,19]

The underlying cause of the variability of measured $\theta$ values outlined above has been attributed to a variety of experimental challenges. The first challenge is that direct methods of bringing small droplets of $CO_2$ in contact with a mineral surface immersed in water within a high-pressure cell are arduous and susceptible to systematic error associated, for example, with the choice of fluid−fluid pre-equilibration time[26] and with the limits in length-scale of measurement or resolution, particularly at $\theta$ values close to zero.[27,28]

The second challenge is that surface roughness can significantly impact the measured $\theta$ values but is difficult to control and ubiquitous in experimental samples.[21,29,30] Young's contact angle, which can be related to interfacial tensions and will be discussed in detail in later sections, assumes an ideal smooth and homogeneous surface, and as such, it can only be measured with significant uncertainty.

The third challenge is the difficulty of avoiding contamination by impurities that can confer surface roughness or modify interfacial energies in the mineral−water−$CO_2$ system. Efforts to minimize impurities are often inconsistent and a source of discrepancy, particularly at the high temperature and pressure conditions of GCS.[12,31] Among studies that used more stringent methods of cleaning, questions arise as to whether the cleaning method altered the surface and whether contamination still occurred.[22,27,32−34]

Finally, the fourth challenge is the existence of confounding factors that arise when measuring $\theta$ values using advancing or receding droplets. Typically, the $\theta$ values measured when the fluid−fluid interface is advancing can vary substantially, up to 40°, from those measured when receding.[20,25,29] Different trends with pressure and temperature for advancing and receding $\theta$ values have also been observed.[27] This hysteresis complicates measurements and exhibits poor reproducibility.[29] Surface contamination and roughness may play a role in this hysteresis, as may the existence of the adsorbed or residual water films at mineral−$CO_2$ interfaces,[31,35,36] although some of it appears to originate from the atomistic nature of the solid surface.[37]

A recurrent question that underlies several of the challenges outlined above is the relationship between macro- and nanoscale manifestations of wetting and capillarity. At the macroscale (Figure 1a), the contact angle is determined by the interfacial energies of the three isolated interfaces ($\gamma_{sg}$, $\gamma_{sw}$, and $\gamma_{gw}$ for the $CO_2$−solid, water−solid, and $CO_2$−water interfaces) as described by Young's equation

$$\gamma_{sg} = \gamma_{sw} + \gamma_{gw} \cos\theta \quad (1)$$

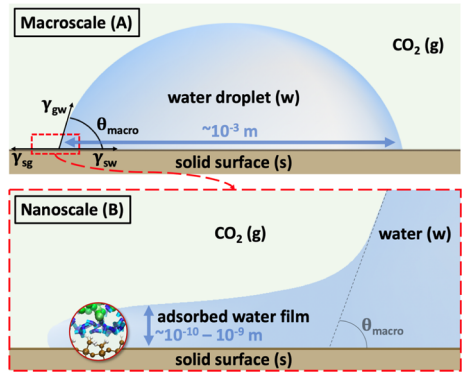


**Figure 1.** Conceptual representation of a system containing water and $CO_2$ on a solid surface. Experimental measurements of the contact angle are typically made (A) at the macroscale (upper panel) using droplets with radii as small as a few mm. (B) At the nanoscale (lower panel), the evaluation of the contact angle is complicated by the existence of adsorbed water films with thickness on the order of a few nm.

Similarly, the radius of curvature $R$ of the $CO_2$−water interface is determined by the interfacial energy and by the bulk fluid pressures on both sides of the interface ($P_g$, $P_w$) as described by the Young−Laplace equation

$$R = \gamma_{gw}/(P_g - P_w) \quad (2)$$

At the nanoscale (Figure 1b), $\theta$ and $R$ necessarily diverge from the predictions of eqs 1, 2 because of the interactions between the fluid−fluid interface and the solid surface.[38,39] These interactions have been studied particularly in the context of water vapor adsorption[40] and are often represented using the concept of disjoining pressure $P_{disj}$, a repulsive pressure between the fluid−fluid and fluid−solid interfaces that varies with film thickness $h$.[41] Theoretical studies have noted that adsorbed films may hold the key to resolving many of the issues outlined above.[35,42−48] Unfortunately, the relationship between macro- and nanoscale manifestations of wettability remains incompletely understood, largely because of the difficulty of experimentally observing the transition from the droplet to film.[35]

Molecular dynamics (MD) simulations have shown promise as a complementary technique to elucidate wetting and capillary phenomena at the nanoscale.[37,49−51] These simulations probe length scales of $\sim 10^{-10}$ to $10^{-7}$ m as required to examine the transition from bulk fluids to thin films illustrated in the lower panel of Figure 1. Furthermore, they enable studying idealized systems with perfectly controlled roughness, chemistry, and fluid flow and can provide direct information on the importance of different types of atomistic−level interactions. To date, applications of MD simulations to wettability and multiphase flow in GCS conditions remain relatively sparse.[52−56] Existing studies have focused mostly on the $\theta$ values of quartz or silica by water versus $scCO_2$ and have shown that these values can vary from 0 to 85° depending on the system set-up and geometry, surface silanol site density, equilibration time, and the choices of interatomic potential parameters.[55,57−63]

As noted above, previous MD simulation studies of quartz−water−$scCO_2$ systems focused primarily on predicting $\theta$ in order to help resolve the spread of the experimental database. In the present study, instead, we focus more broadly on gaining insights into wetting and capillary phenomena. In particular,


https://dx.doi.org/10.1021/acs.jpcc.0c07948
J. Phys. Chem. C 2020, 124, 25382−25395

we aim to shed light on the transition from bulk fluids to thin films and on deviations of $\theta$ and $R$ from the predictions of eqs 1, 2. Our methodology is similar to that used in previous studies of quartz−water−$CO_2$ systems but includes three significant advances. First, we carry out relatively long simulations (up to 100 ns), allowing our systems to reach a fully equilibrated state before predicting any properties and enabling a precise determination of the average curvature of the fluid−fluid interface. Second, we calculate the local stress distribution in our simulated systems in a manner that provides nanoscale information on the mechanics of wetting and capillarity. Third, we examine the adsorbed water film at the quartz−sc$CO_2$ interface and its relationship to our predicted $\theta$-values.

Finally, we note that the wettability of mineral surfaces by water versus nonpolar fluids underlies many important phenomena in soil science,[64] atmospheric chemistry,[65] biology,[66] water purification technology,[67] and a variety of other fields.[68,69] Although the present study examines conditions relevant to GCS, our results on the fundamental controls on mineral wettability should be broadly relevant to the other areas of study noted above.

## 2. METHODS

We used the open-source program LAMMPS[70] to carry out MD simulations in the canonical ($NVT$) ensemble. All simulations were carried out at a constant temperature of 318 K using a velocity-Verlet algorithm with a time-step of 1 fs. The simulation cell size was 176.893 × 100.000 × 27.023 Å with periodic boundary conditions in all directions.

In the simulation cells for this study, we defined atomic positions and interactions for a slab of $\alpha$-quartz, 5280 water molecules, and 0−1716 $CO_2$ molecules. The quartz slab has dimensions of 176.893 × 4.044 × 27.023 Å (36 × 8 × 5 unit cells) and forms parallel surfaces in the $x$−$z$ plane spaced 66 Å apart across a slit-shaped nanopore. The width of the pore was selected to enable the existence of a region with bulk fluid-like properties within each fluid phase. The relatively shorter depth of the simulation cell along the $z$ axis was selected to create a system with a fluid−fluid curvature only within the $x$−$y$ plane to avoid impacts of the three-phase line tension on the contact angle.[56,71] Water and $CO_2$ molecules were inserted in the pore space as two distinct phases with flat $CO_2$−water interfaces initially oriented in the $y$−$z$ plane, normal to the quartz surfaces. Water molecules occupy roughly half of the pore space in all the simulations, and the number of $CO_2$ molecules is used to control the system pressure. The simulations were carried out with 0, 214, 429, 858, 1075, 1288, 1502, and 1716 $CO_2$ molecules to achieve bulk $CO_2$ pressures ranging from about 0 to 12 MPa, above which $CO_2$ density and $CO_2$−water interfacial tension approach a plateau.[72] In the system with 0 $CO_2$, the bulk $CO_2$ pressure of 0 MPa refers to the rounded absolute pressure (~0.003 ± 0.002 MPa) in the bulk gas region of the bubble defined in the same way as for systems with $CO_2$ but can also be thought of as 0 partial pressure of $CO_2$. While the gas phase pressure is never exactly 0 MPa, it is on the order of 0.01 MPa and small enough to be approximated as 0 MPa for our purposes. Figure 2 illustrates the geometry of the simulated systems.

The quartz unit cell was based on X-ray diffraction analyses by Kihara.[73] The surface was prepared by cutting the bulk quartz lattice along the most stable natural "termination $\beta$" $(10\bar{1}0)$ plane,[74] then attaching protons and hydroxyls to the resulting undercoordinated oxygens and silicons, respectively, to approximate low pH conditions[75] and allowing them to relax over a short NVE simulation. Quartz atoms were held rigid during subsequent production runs with the exception of the surface hydroxyl groups. This method resulted in a surface with 720 silanol hydroxyl groups, or a surface silanol site density of 7.53 OH per nm$^2$, and a neutral surface charge. Atomistic studies of silica are often based upon the Zhuravlev model, which predicts a lower surface silanol site density.[76] Though silica surface silanol site densities are not applicable for the quartz model used in this study, it is important to note that quartz surface silanol site densities are likely higher than those used in silica simulations and experiments, and those present in many practical applications.[77−79]

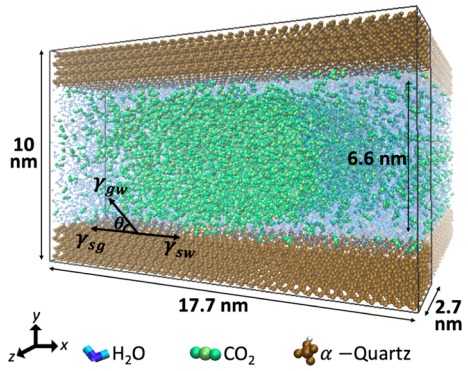


**Figure 2.** Snapshot of the system containing 1716 $CO_2$ molecules. Other simulated systems were identical but contained fewer $CO_2$ molecules. The MD simulation cell is outlined in black; periodic images in the $z$ direction are visualized to highlight the tubular conformation of the $CO_2$ bubble.

Our MD simulations numerically solve Newton's equations of motion for a many-particle system using semiempirical interatomic potential parameters. For the main simulations in this study, we employed the CLAYFF model for quartz,[80] the extended simple point charge (SPC/E) model for water,[81] and the EPM2 model for $CO_2$.[82] Interactions between unlike atoms were calculated using the Lorentz−Berthelot combining rules, with the exception of the interactions between $CO_2$ and water or quartz O atoms, for which we tested an array of options including the PPL model.[83] The main results presented in this paper use the PPL model for these intermolecular interactions. This combination of models has previously been found to accurately describe the structure and dynamics of water in its bulk liquid form (including at high pressures),[84−86] on the quartz $10\bar{1}0$ surface,[87,88] and in silica nanopores[88,89] and the vapor−liquid coexistence curve of pure $CO_2$.[90,91] It also provides one of the best predictions of water's liquid−vapor interfacial tension[92] and of the pressure dependence of $CO_2$−water interfacial tension.[52] Water molecules were kept rigid using the SHAKE algorithm,[93] while $CO_2$ molecules were modeled as flexible using the parameters of EPM2 with a harmonic constant taken from Yu et al.[94] Short-range Coulomb and van der Waals interactions were truncated at 12 Å. Long-range Coulomb interactions were treated by three-dimensional PPPM Ewald summation.[95] All interatomic interaction parameters are given in Table S1.

All simulations were initialized using a brief run in the microcanonical ($NVE$) ensemble. Equilibrium configurations were then reached by running the simulation in the canonical ($NVT$) ensemble at 318 K for 20 ns, after which bulk fluid


https://dx.doi.org/10.1021/acs.jpcc.0c07948
J. Phys. Chem. C 2020, 124, 25382−25395

properties were isotropic and the water film between the quartz and $CO_2$ reached an equilibrium thickness (Figure 3).

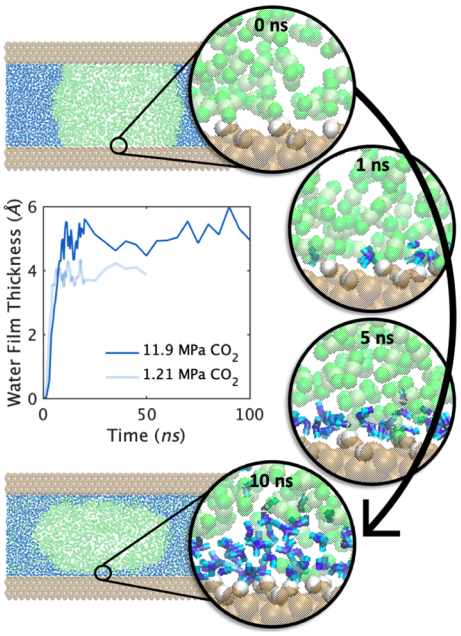


**Figure 3.** Snapshots of the system containing 1716 $CO_2$ molecules during the first 10 ns of equilibration in the *NVT* ensemble. The figures on the right show the progressive growth of the water film at the quartz−$CO_2$ interface. Equilibration was determined to be complete when bulk fluid properties became isotropic and the water film stopped growing.

These timescales necessary for equilibration have also been observed in previous MD simulation studies[96] but have not been employed in most reference MD studies of quartz−water−sc$CO_2$ systems to date. A more detailed analysis of equilibrium time scales is provided in Figures S2 and S3. Finally, each system was simulated for an additional 20−80 ns to sample its equilibrium properties. The temperature was kept constant using a Nosé−Hoover thermostat with a coupling constant of 1 ps.

Time-averaged maps of the densities and stresses were evaluated every 5 ns from the data recorded every time-step as a function of the $x-y$ coordinates using a 1 × 1 Å resolution. For each of these time-averaged maps, the $CO_2$ bubble was approximately centered post-simulation for analysis. Bulk fluid regions were defined as 20 × 40 Å regions in the $xy$ plane located at least 15 Å away from any interface and displaying an isotropic stress tensor. The latter implies minimal interfacial effects in these regions. The bulk region stress tensors were averaged spatially and over each 5 ns of production after equilibration to give a bulk pressure. Normalization of this region to the middle of the fluid phases and at a minimum distance from each interface accounts for any fluid movement. Averaging over several nanoseconds accounts for bubble shape fluctuations. Confidence intervals on all reported simulation results correspond to the statistical uncertainty $\pm 2\sigma/\sqrt{n}$, where $\sigma$ is the standard deviation calculated from $n$ independent estimates obtained by dividing each 20−80 ns simulation into segments of 5 ns.

## 3. RESULTS & DISCUSSION

**3.1. Structural Properties—Water Density on the Quartz Surface.** Atomic density maps of water atoms in each simulation were examined to determine the density distribution of water near the quartz surface, the location of the quartz−water interface, and the thickness of the adsorbed water film. In particular, we calculated one-dimensional density profiles in the direction normal to the quartz surface ($y$) across the bulk water region (in a 40 Å-wide region located >20 Å away from the $CO_2$−water interfaces) and across the $CO_2$ bubble (in a 20 Å-wide region across the center of the bubble). Representative water density profiles in the $y$ direction are shown in Figure 4 for the system with $P_g$ = 7.9 MPa.

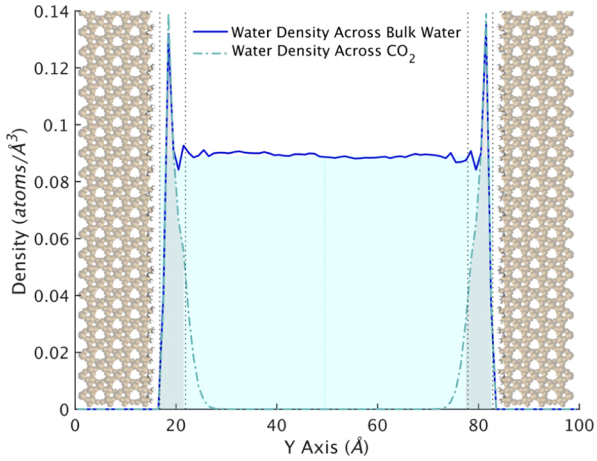


**Figure 4.** Water atomic density profiles in the direction normal to the quartz surface ($y$) calculated across the bulk water or bulk $CO_2$ regions (solid and dot-dashed blue lines). The vertical dotted lines mark the locations of the quartz−water and $CO_2$−water interfaces defined as Gibbs dividing surfaces using water as a reference phase. The blue shading shows the density of bulk water. The gray shading shows the film of water between the quartz and $CO_2$.

Water density profiles at the quartz−water interface (solid blue line in Figure 4) show a peak located 3 ± 0.5 Å above the average height of the silanol O atoms followed by smaller peaks at 6 ± 0.5 and 10 ± 0.5 Å above the silanol O atoms. The ∼3 Å spacing between these peaks suggests that they correspond to the first, second, and third water monolayer on the quartz surface. Water density layering is observed only within ∼10 Å from the interface, in agreement with previous studies.[97] The location of the quartz−water interface, calculated using Gibbs' definition (i.e., as the interface location yielding a zero surface excess of water), is indicated by the vertical dotted lines at $y$ = 17.1 and 83.0 Å. This interface is located 1.6 Å above the silanol O atoms in agreement with the 1.5 Å radius of O atoms.

Water density profiles across the quartz−$CO_2$ interface (dot-dashed blue line in Figure 4) show the existence of an adsorbed water film. This is expected as evenly distributed surface silanol groups have been shown to stabilize a surface water layer.[98,99] The density profile of water in this film displays a peak matching that of the first water layer at the quartz−bulk water interface and a shoulder located at the same height as the second water layer. The average thickness of the film, calculated using Gibbs' definition, ranges from 3.7 to 5.1 Å depending on the number of $CO_2$ molecules in the system. These observations reveal that the adsorbed water film at the quartz−$CO_2$ interface has a thickness of ∼1.5 water


https://dx.doi.org/10.1021/acs.jpcc.0c07948
J. Phys. Chem. C 2020, 124, 25382−25395

monolayers and that the structure of the first water layer in this film is similar to that of water at the quartz−bulk water interface.

**3.2. Structural Properties—$CO_2$ Density on the Water Surface.** Density maps of water atoms were further examined to determine the location of the $CO_2$−water interfaces. At the flat $CO_2$−water interface (i.e., the interface between the water film and the $CO_2$ phase), the interface location was calculated by adding the water film thickness to the location of the quartz−water interface obtained as described in the previous section. Along the pore mid-plane, the $CO_2$−water interface location was calculated using Gibbs' definition as described in the previous section. Finally, the shape of the curved $CO_2$−water interface was approximately evaluated using the locations where the average water density equaled half of that of bulk water. The resulting interface locations are overlain on an *xy* map of $CO_2$ density for the system with $P_g$ = 7.9 MPa in Figure 5.

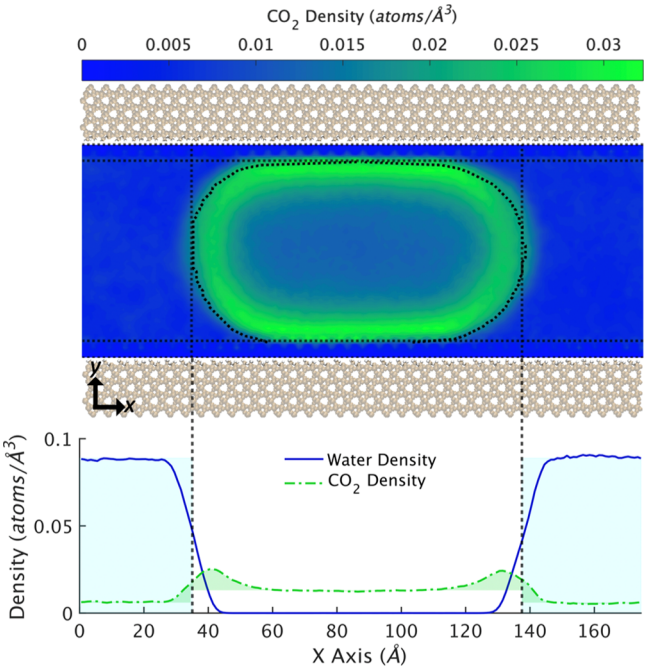


**Figure 5.** Upper panel: $CO_2$ density map in the simulation with $P_g$ = 7.9 MPa. The straight dotted lines show the locations of the Gibbs dividing surfaces of water at the quartz−water film and water film−$CO_2$ interfaces (horizontal lines) and at the pore mid-plane (vertical lines). The curved dotted lines show locations where water density equals half of that of bulk water at the curved $CO_2$−water interface. Lower panel: water and $CO_2$ atomic density profiles calculated in a 10 Å wide region along the pore mid-plane. The water density (used to locate the interface) is shown as a blue line with shaded blue areas indicating bulk water density. The $CO_2$ density (used to calculate the surface excess of $CO_2$) is shown as a dot-dashed green line. The shaded green regions show $CO_2$ density in excess of the bulk and dissolved concentrations.

Atomic density maps of $CO_2$ reveal the existence of a region of enhanced $CO_2$ density adjacent to the water surface (bright green region in the upper panel in Figure 5). Density profiles calculated across the center of the $CO_2$ bubble in the *x* and *y* directions (Figures 5 and S4) show that this enhanced $CO_2$ density reflects the existence of a significant $CO_2$ surface excess, $\Gamma_g$, in agreement with previous experimental and simulation studies.[52,57,100−102] The predicted values of $\Gamma_g$ at the curved $CO_2$−water interface, on the adsorbed water film, and in separate simulations of a flat $CO_2$−water interface (with no quartz) are shown in Figure 6 as a function of bulk $CO_2$ pressure, $P_g$. The values of $\Gamma_g$ at the curved $CO_2$−water interface are calculated using radial coordinates to account for the curvature of this interface.

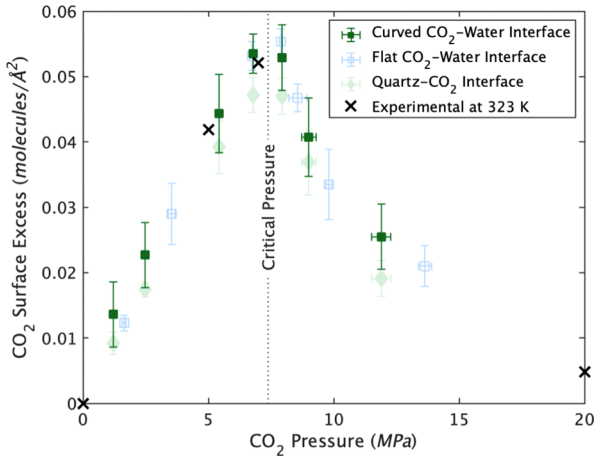


**Figure 6.** Surface excess of $CO_2$ on various water surfaces as a function of bulk $CO_2$ pressure. Green and blue symbols show MD results obtained at 318 K for the curved $CO_2$−water interface (dark green filled squares), the water−coated quartz−$CO_2$ interface (light green filled diamonds), and a flat $CO_2$−water interface simulated separately with no quartz (light blue squares). Black cross symbols show results at 323 K reconstructed from experimentally measured interfacial energies.[52,105] The vertical line shows the critical pressure of $CO_2$. Reconstructed values just above the critical pressure are not shown as they are highly sensitive to the fitting method.

Overall, our results show that the adsorption of $CO_2$ on the water surface is highly sensitive to $CO_2$ pressure. It peaks near the critical pressure of $CO_2$ (7.4 MPa) in agreement with previous studies of $CO_2$ adsorption in nanoporous materials[103,104] and at flat $CO_2$−water interfaces.[52] The method used to calculate surface excess from experimentally measured interfacial energies was described by Nielsen et al.[52] at ranges much above the critical temperature and is reproduced here from the same experimental data set[105] at a lower temperature. A comparison with the experimental and MD simulation results obtained at 383 K shows that the peak surface excess determined at 318 K is much more obviously related to the critical pressure and more sensitive to our choice of fitting method, as expected because of the much greater proximity of our simulated conditions to the critical temperature of $CO_2$ (304 K). A comparison of the green and blue data sets, as shown in Figure 6, shows that the adsorption of $CO_2$ on the water surface is not significantly impacted by the curvature of the fluid−fluid interface in our simulated system and may be mildly inhibited on the surface of the adsorbed water film, perhaps reflecting a lower solubility of $CO_2$ in the water film than in bulk liquid water.

**3.3. Structural Properties—Curvature of the $CO_2$−Water Interface.** Detailed analyses of the water density maps were carried out to evaluate the shape of the curved $CO_2$−water interface. Briefly, for each 5 ns of simulation, we computed a map of water density averaged over the four "corners" of the $CO_2$ bubble. From these maps, we calculated,


https://dx.doi.org/10.1021/acs.jpcc.0c07948
J. Phys. Chem. C 2020, 124, 25382−25395

at each height $y$, the location of the $CO_2$–water interface in the $x$-direction (estimated as the location where water density equaled half the value for bulk water) relative to its location at the pore mid-plane. The results are shown in Figure 7 for the

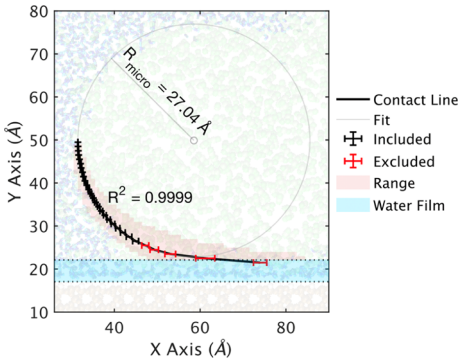


**Figure 7.** Average shape of the $CO_2$–water interface in the $x$–$y$ plane at $P_g$ = 11.9 MPa. At every height $y$, the black and red symbols show the average $x$-coordinate of the fluid–fluid interface. Results are normalized to the $x$-coordinate of the fluid–fluid interface at the pore mid-plane (to correct for random fluctuations in the location of the bubble in the $x$ direction) and averaged over the four corners of the $CO_2$ bubble. The maximum and minimum $x$-coordinates of the fluid–fluid interface are shown as a range in pink. The figure also shows the circle that yielded the best fit to the shape of the interface as described in the text. Black points on the curve were retained by the fitting procedure, while red points were excluded as they decreased the quality of fit.

simulation at $P_g$ = 11.9 MPa; error bars show 95% confidence intervals on the average location of the interface, while the shaded pink area shows the range of interface locations. Our results reveal significant variability in the shape of the interface determined during any 5 ns interval. These fluctuations in interfacial shape have been noted in previous studies both as a challenge in determining wetting properties from short simulations[106] and as a potential source of information on wetting dynamics.[107] Despite these fluctuations, our results show that a precise evaluation of the average shape of the interface is possible using relatively long simulation durations (20–80 ns). Finally, our results show that the transition from the curved $CO_2$–water interface to the surface of the adsorbed water film (shaded blue region in Figure 7) exhibits no obvious deviations from the arc of a fitted circle even in the region potentially associated with the second and third water layers, as shown in Figure 4.

To further analyze the shape of the curved interface, we developed an iterative circle fitting procedure aimed at identifying the optimal circular fit to the shape of the interface. Our procedure consisted of starting with the few points closest to the pore mid-plane (which should exhibit the behavior most consistent with eq 2) and finding the circle that provided the best fit to these points (i.e., iteratively minimizing the approximate mean square distance for the points and for the center coordinate based on the Taubin method,[108] building on a code by Chernov[109]). Then, our procedure progressively increased the number of points used in the circle fitting algorithm by including points located closer and closer to the quartz surface. For each circle fitted to a set of points, we then calculated a coefficient of determination, $R^2$, based on the $x$-coordinate fit as a characterization of the circularity of the included points. For all simulated systems, the results showed a progressive increase in $R^2$ as the fit was extended to within ~7 Å of the quartz surface, followed by a rapid decrease in $R^2$ as the fit was extended even closer to the surface. The best-fitting circle was identified as the one that yielded the highest $R^2$ value while using at least five points. The radii of curvature from these best-fitting circles are henceforth referred to as $R_{micro}$. The resulting best fit in the case of the simulation at $P_g$ = 11.9 MPa is illustrated in Figure 7. As shown in Figure 7, the average shape of the fluid–fluid interface is remarkably well-described by a hemicircular cap. This description holds well for all portions of the fluid–fluid interface located more than one water layer away from the surface of the adsorbed water film at all pressures. Furthermore, the best-fitting circular cap was found to be tangential to the surface of the film in all simulated systems, that is, the contact angle obtained based on the nanoscale curvature of the fluid–fluid interface is essentially zero at all pressures.

**3.4. Stress Tensor Properties—Bulk Fluid Pressures and Capillary Pressure.** Our predictions on the pressure of bulk $CO_2$ and water ($P_g$ and $P_w$) as a function of $CO_2$ density are shown in Figure 8. Values reported for bulk $CO_2$ were

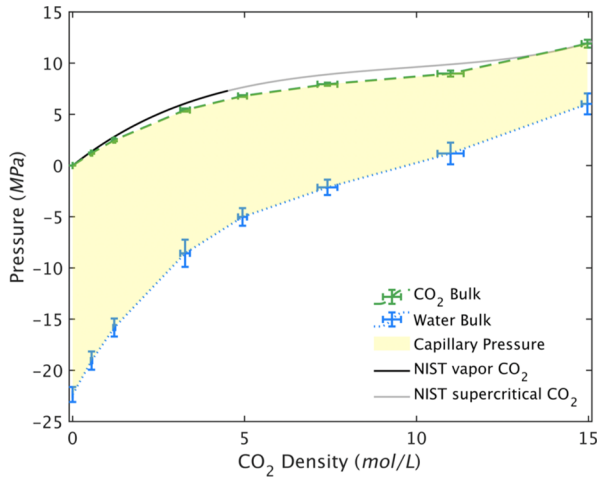


**Figure 8.** Pressure of bulk $CO_2$ and water in our simulated systems as a function of the density of bulk $CO_2$. The vertical offset between the two curves equals the capillary pressure. The NIST standard equation of state for $CO_2$ at 318 K is shown as a solid black and gray line.[110]

corrected from the raw LAMMPS output to account for the redundancy of one of the rotational degrees of freedom in the linear $CO_2$ molecule, as described in the Supporting Information. Comparison of our predicted $P_g$ values with the National Institute of Standard and Technology (NIST) data on the density of bulk $CO_2$ at 318 K indicate that our simulations reasonably capture the equation of state of $CO_2$, including the transition from gas to supercritical fluid. The results on $P_w$ show that pressure in the bulk water phase is negative in the absence of $CO_2$, indicating that a suction is created with a value close to that expected for a water meniscus stretched between two perfectly hydrophilic surfaces in a 66 Å wide nanopore in the absence of adsorbed water films at 318 K ($P_w = -\gamma_{gw}/R_{micro} = -20.5$ MPa). With increasing $CO_2$ density, $P_w$ progressively increases in a manner that reflects the evolution of external stresses on the water meniscus (i.e., tensile stress imposed by the quartz surface and compressive stress imposed by the $CO_2$ phase).


https://dx.doi.org/10.1021/acs.jpcc.0c07948
J. Phys. Chem. C 2020, 124, 25382–25395

The vertical offset between the two curves, as shown in Figure 8, provides a direct measure of the capillary pressure $P_{cap} = P_g - P_w$ in our simulations. As shown in the figure, the $CO_2$ phase is consistently overpressured relative to the water phase in agreement with observations that water is the wetting phase in our simulations (Figure 3). Predicted values of $P_{cap}$ decrease from 22.4 to 5.9 MPa as $CO_2$ density increases from 0 to 15 mol $L^{-1}$, indicating that $CO_2$ should invade water-filled silica nanopores more readily at higher $CO_2$ densities. A part of this effect can be attributed to the fact that the $CO_2$−water interfacial tension ($\gamma_{gw}$ in eq 2) decreases significantly with increasing $CO_2$ density as discussed further below.[52]

**3.5. Stress Tensor Properties—Disjoining Pressure in the Thin Film.** As noted long ago by Derjaguin,[111] for systems such as that studied here, where a curved fluid−fluid interface coexists with a thin adsorbed film at equilibrium, the capillary pressure $P_{cap}$ measured between the two bulk fluid phases equals the disjoining pressure $P_{disj}$ in the adsorbed fluid film. This equality can be demonstrated, for example, by using the relationship between disjoining pressure and water activity in an adsorbed water film

$$P_{disj} = -\frac{R_{igc}T}{V_m}\ln(a_w) \tag{3}$$

where $R_{igc}$ is the ideal gas constant, $T$ is the absolute temperature, $V_m$ is the molar volume of water, and $a_w$ is the water activity. An analogous expression at the curved fluid−fluid interface is the Kelvin equation

$$\ln(a_w) = \frac{\gamma_{gw}V_m}{RR_{igc}T} \tag{4}$$

where $R$ is the macroscale radius of curvature defined in the introduction. If the system is at equilibrium, the activity of water in the film equals that in the meniscus and the combination of eqs 2−4 yields $P_{disj} = P_{cap}$.

Predicted values of $P_{disj}$ in our simulations are shown in Figure 9 as a function of water film thickness $h$. Our prediction that $P_{disj} > 0$ is consistent with the observed existence of a stable adsorbed water film on the surface of quartz and other silicate minerals in the presence of humid $scCO_2$.[54,57,112,113] Overall, our results on water film thickness $h$ versus $P_{disj}$ are broadly consistent with previous studies. For example, Clarke and Gee[114] reported $P_{disj}$ values of 3.5−7.0 MPa for 5 Å-thick films of *n*-alkanes on quartz. For water films on quartz in the absence of $CO_2$, the measured film thicknesses show significant scatter,[40,41,115] perhaps due to differences in surface roughness and the degree of deprotonation of surface silanol groups (both of which would tend to promote thicker films). However, the smallest values reported in both experimental and theoretical studies are on the order of ∼5 Å at a $P_{disj}$ value of 10 MPa,[116−119] in agreement with our results.

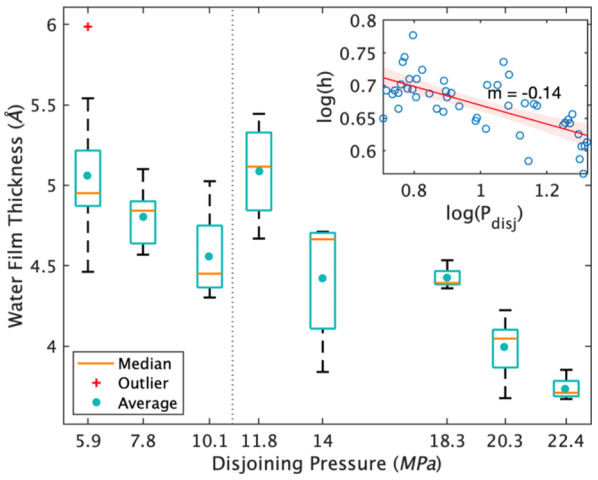


**Figure 9.** Thickness of the adsorbed water film as a function of disjoining pressure. The inset shows values of $\log(h)$ vs $\log(P_{disj})$ obtained during 5 ns intervals of each simulation along with the best fitting linear regression (red line). The vertical line shows the boundary between gaseous and $scCO_2$.

Strongly hydrophilic surfaces (i.e., surfaces with $\theta = 0$) are expected to develop an infinitely thick adsorbed water film as water activity approaches 1. According to various theoretical models, the relationship between $P_{disj}$ and $h$ should follow an inverse power law relation $P_{disj} \propto h^{-b}$ with $b = 1-3$.[41] Conversely, on surfaces with $\theta > 0$, $P_{disj}$ should approach zero at a finite film thickness. The results presented in Figure 9 are insufficient to evaluate whether $P_{disj}$ approaches zero at an infinite or finite film thickness. A plot of $\log(P_{disj})$ versus $\log(h)$ during 5 ns intervals of each simulation suggests that our results are consistent with inverse power-law relation with $b = 6.9 \pm 2.2$, and disjoining pressure decays more rapidly than expected with increasing film thickness.

**3.6. Stress Tensor Properties—Surface Tension at the Curved $CO_2$−Water Interface.** The interfacial tensions between the bulk $CO_2$ and water phases in our simulations were calculated from the maps of the average local stress tensors by applying the Irving−Kirkwood formula[102,120]

$$\gamma_{gw} = \int_{-\infty}^{+\infty}[p_N(x) - p_T(x)]dx \tag{5}$$

where $p_N$ and $p_T$ are the local stresses in directions normal and tangential to the interface and $x$ is distance across a single fluid−fluid interface. We evaluated $(p_N - p_T)$ in a 10 Å wide region along the pore mid-plane and calculated the integral using the trapezoidal method with unit spacing. A representative profile of the stress anisotropy in the case of the simulation at $P_g = 7.9$ MPa is shown in Figure S5 and the resulting values of $\gamma_{gw}$ are shown in Figure 10. For comparison, values of $\gamma_{gw}$ obtained using MD simulations of a flat $CO_2$−water interface (with no quartz) are also reported in Figure 10 along with the experimental results previously identified as a high quality data set.[52,105]

As shown in Figure S5, the local stresses near the center of the water and of the $CO_2$ bubble are isotropic. This suggests that these regions are bulk fluid-like despite the small distance to the nearest interface (≤30 Å). In contrast, the local stresses in the vicinity of the $CO_2$−water interface are highly anisotropic, as expected based on the significant $CO_2$−water interfacial energy.[102] The magnitude of the stress anisotropy correlates roughly with the spatial gradient in water density, in agreement with the expectation that the $CO_2$−water surface tension originates largely from the disruption of the water hydrogen bond network at the interface.

The values of $\gamma_{gw}$ shown in Figure 10 are consistent with previous observations. In the absence of $CO_2$, the surface of liquid water has a high interfacial energy ($\gamma_{gw} = 67.9$ mN $m^{-1}$ at 323 K)[121] that is underestimated by the SPC/E water model ($\gamma_{gw} = 59.8$ mN $m^{-1}$ at 318 K according to our simulation). The difference between experiments and simulations (≈8 mN


https://dx.doi.org/10.1021/acs.jpcc.0c07948
J. Phys. Chem. C 2020, 124, 25382−25395

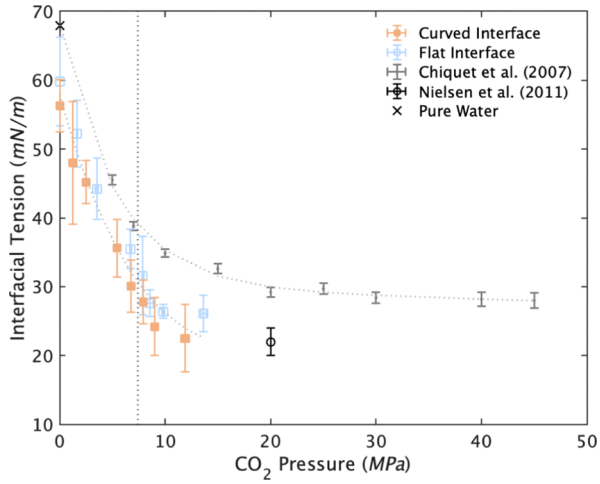


**Figure 10.** Predicted $CO_2$–water interfacial tension as a function of bulk $CO_2$ pressure in the system with quartz and a curved fluid–fluid interface (orange filled squares) and in the system with a flat fluid–fluid interface and no quartz (light blue squares). Experimental data at ~323 K obtained by Chiquet et al. are shown in gray.[105] Points for each are fitted exponentially (dotted curves). The measured surface tension of water at 323 K (67.94 mN $m^{-1}$)[121] is shown as a black cross. A previous simulation prediction obtained by Nielsen et al. at 323 K using the same interatomic potential models is shown as a black circle.[52] The vertical line shows the critical pressure of $CO_2$.

$m^{-1}$) is identical to that reported in previous studies.[92] With increasing $CO_2$ pressure, the surface tension of water decreases to ~30 mN $m^{-1}$ with a clear inflection near the critical pressure of $CO_2$. The combination of the SPC/E water model, the EPM2 $CO_2$ model, and the PPL model of $CO_2$–water interactions correctly predicts the pressure dependence of $\gamma_{gw}$, as previously observed at 383 K.[52]

The dependence of $\gamma_{gw}$ on pressure (or rather fugacity) is determined by the $CO_2$ surface excess through the Gibbs adsorption equation[122]

$$d\gamma_{gw} = -R_{igc}T\Gamma_g \, d[\ln(f_g)] \quad (6)$$

where $f_g$ is the fugacity of $CO_2$. Therefore, the agreement between experimental and simulation results on the pressure dependence of $\gamma_{gw}$, as shown in Figure 10, suggests that our simulations accurately predict the $\Gamma_g$ values shown in Figure 6.

**3.7. Young–Laplace Behavior Near the Three-Phase Contact Line—Macro- Versus Microscale Curvature.** As noted in the Introduction, the Young–Laplace equation gives accurate continuum scale predictions of the capillary pressure difference in systems with smooth surfaces. Previous studies have proposed that this relationship can be used to characterize capillary effects in MD simulations, regardless of the nanoscale interfacial curvature.[123] Following this approach, we used our values of $P_c$ and $\gamma_{gw}$ (Figures 8 and 10) with the Young–Laplace equation (eq 2) to calculate a "macroscale" radius of curvature $R_{YL}$. The resulting radius is entirely independent of the observed "microscale" radius of curvature $R_{micro}$ presented in Section 3.3 (Figure 7). A comparison of the two measures of curvature provide insights into the validity of the continuum-scale relations (eqs 1, 2) in the vicinity of the solid surface.

As the first comparison of $R_{YL}$ and $R_{micro}$, we carried out a similar circle-fitting analysis as in Section 3.3 but with the radius of curvature constrained to $R_{YL}$. We analyzed both the regressive statistics and the residuals to determine which points on the averaged curve fit well to a circle with radius of curvature $R_{YL}$ (Figure 11). The points that clearly skewed

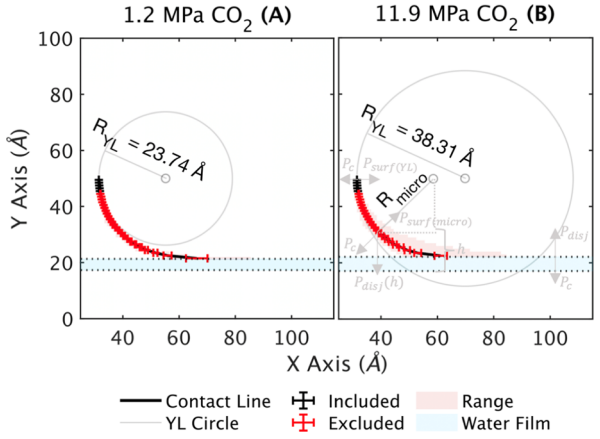


**Figure 11.** Same as Figure 7 but with a radius of curvature constrained to match the capillary pressure difference between $CO_2$ and water based on the Young–Laplace equation. The figures shown are the simulations at (A) 1.2 MPa (where $R_{YL} < R_{micro}$) and at (B) 11.9 MPa (where $R_{YL} > R_{micro}$).

toward one side of the circle were interpreted as deviating from the expected curvature predicted by the Young–Laplace equation. Our results show that $R_{YL}$ is smaller than $R_{micro}$ at low pressures (Figure 11a) and progressively grows with increasing pressure until it meets and then surpasses $R_{micro}$ (Figure 11b). Our circle fitting with $R_{YL}$ suggests that the continuum-scale approximation used in the Young–Laplace equation breaks down closer than approximately 20 Å from the solid surface. Both $R_{YL}$ and $R_{micro}$ values are presented in Table S2.

As the second comparison of $R_{YL}$ and $R_{micro}$, we used both values to calculate the contact angle $\theta$ using the geometric relation $\theta = \cos^{-1}(P_{cap}R/\gamma_{gw})$ every 5 ns. The results, as presented in Figure 12, show that both definitions of $R$ are consistent with a contact angle of 0° below the critical pressure of $CO_2$. Above the critical pressure, however, $R_{micro}$ still suggests $\theta = 0°$, whereas $R_{YL}$ implies contact angles up to 42 ± 14°. Interestingly, the divergence between the two sets of $\theta$ values, as shown in Figure 12, reflects that observed in the experimental database on the wettability of stringently cleaned quartz surfaces, where certain studies report near-zero $\theta$ values regardless of $P_g$,[18,24,58] whereas other studies report near-zero $\theta$ values at low pressures increasing to ~20–50° at supercritical $P_g$ values.[13,23,25,26,30,31,62,124–126]

**3.8. Young–Laplace Behavior Near the Three-Phase Contact Line—Link between Disjoining Pressure and Fluid–Fluid Interfacial Curvature.** The results discussed in the previous section and summarized in Figure 11 suggest that the solid surface may impact the shape of the fluid–fluid interface up to distances of at least 20 Å, as the radii of curvature predicted by the Young–Laplace equation fit mainly to points approximately 20 Å and over from the quartz surface (Table S2). This relatively long-ranged impact is consistent with previous experimental observations that show a similarly long-ranged impact of pore walls on $scCO_2$ density in silica nanopores.[103] It is also consistent with previous MD simulation studies that show the decay length scale of $CO_2$ density accumulation near the $CO_2$–water interface ap-


https://dx.doi.org/10.1021/acs.jpcc.0c07948
J. Phys. Chem. C 2020, 124, 25382–25395

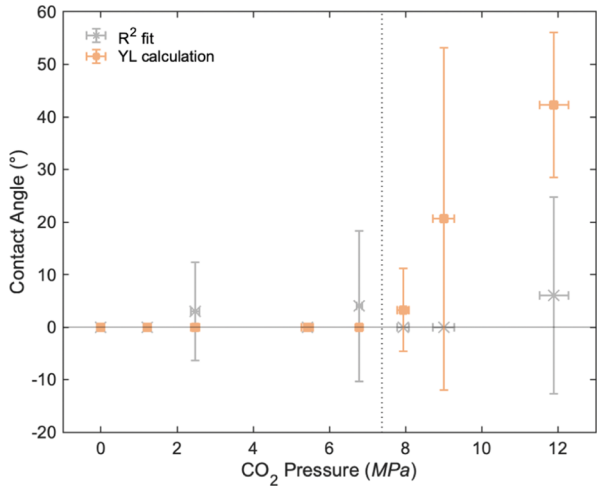


**Figure 12.** Predicted contact angles as a function of bulk $CO_2$ pressure. The two data sets show values calculated from the best iterative fit to the averaged $CO_2$–water interface and trigonometric relationships (grey crosses) and from the capillary pressure difference between $CO_2$ and water with the Young–Laplace equation (orange filled squares). The vertical line shows the critical pressure of $CO_2$.

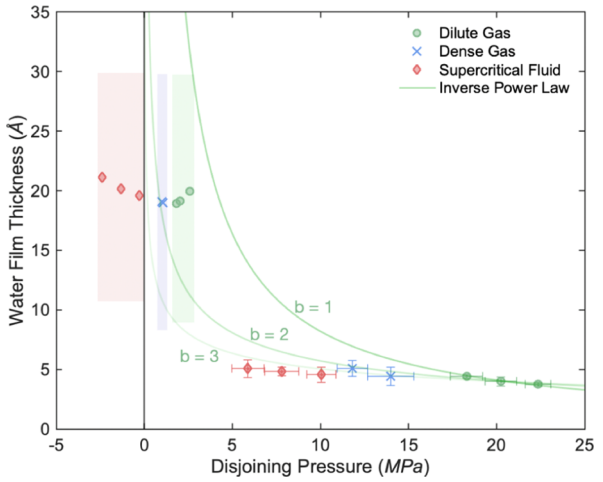


**Figure 13.** Film thicknesses plotted as a function of disjoining pressure from the thin film analysis, as shown in Figure 9, and values of disjoining pressure at the curved interface obtained using the augmented Young–Laplace equation. The results are grouped into three categories based on $P_g$: dilute gas at low $P_g$ (green circles), dense gas (blue crosses), and supercritical fluid at high $P_g$ (red diamonds). The green lines show that inverse power law fits to the three values of $P_{disj}$ in the thin film in the dilute gas region obtained with $b$ = 1, 2, or 3.

proaches infinity near the critical pressure, which again suggests long-ranged impacts of solid surfaces on $scCO_2$.[101] Unfortunately, these long-ranged impacts present a challenge in accurately quantifying the macroscopic quartz–$CO_2$–water contact angle $\theta$ using typical MD simulation cell dimensions.

As noted in previous wettability studies, a dependence of $\theta$ on the length scale of observation is in fact expected if disjoining pressure $P_{disj}$ has a long-ranged impact on the curved fluid–fluid interface.[35,48,127] This phenomenon is illustrated in Figure 11b, where the forces at the fluid–fluid interface are conceptually represented at several locations along the interface. At the pore mid-plane and at the surface of the adsorbed film, this balance involves only two contributions, whereas in the "corner" of the $CO_2$ bubble it involves three phenomena: the capillary pressure difference between the two bulk fluids ($P_{cap} = P_g - P_w = \gamma_{gw}/R_{YL}$), capillary stresses at the curved fluid–fluid interface at a distance $h$ from the surface [$\gamma_{gw}/R_{micro}(h)$], and disjoining pressure at a distance $h$ from the surface [$P_{disj}(h)$]. According to the well-known augmented Young–Laplace equation, this balance can be expressed as[42]

$$P_{cap} = \frac{\gamma_{gw}}{R_{YL}} = \frac{\gamma_{gw}}{R_{micro}(h)} + P_{disj}(h) \tag{7}$$

The augmented Young–Laplace equation gives the overall curvature calculated over a range of distances that are difficult for this study to pinpoint exactly, as the calculation involves a large segment of the interface. Thus, the range is reported with large error bars. Application of eq 7 to our results on $R_{YL}$ and $R_{micro}$ in the range of $h$ values used to determine $R_{micro}$ (roughly $h \approx 20 \pm 10$ Å) yields $P_{disj}(h \approx 20 \pm 10$ Å) = 1.8, 2.6, 2.0, 1.1, 1.0, −0.3, −1.3, and −2.4 MPa at $P_g$ = 0, 1.2, 2.5, 5.4, 6.8, 7.9, 9.0, and 11.9 MPa. These values of $P_{disj}$ are compared in Figure 13 with the values obtained in the thin film (from Figure 9). The values of $P_{disj}$, as shown in Figure 13, are grouped in three ranges of $P_g$: dilute gas ($P_g$ = 0–2.5 MPa), dense gas ($P_g$ = 5.4–6.8 MPa), and supercritical fluid ($P_g$ > 7.9 MPa).

As shown in Figure 13, for dilute or dense $CO_2$ our results are consistent with $P_{disj} > 0$ at all $h$ values (which implies perfectly hydrophilic behavior, $\theta$ = 0), and the relation between $P_{disj}$ and $h$ is consistent with an inverse power law ($P_{disj} \propto h^{-b}$) with $b \sim 1$–3, in agreement with theoretical predictions.[41] For $scCO_2$, however, $P_{disj}$ goes from positive to negative values with increasing film thickness, as expected for a system with partial wetting ($\theta > 0$).[36]

**3.9. Young–Laplace Behavior Near the Three-Phase Contact Line—Impact of the Water Film on the Macroscopic Contact Angle.** Additional insights into the pressure dependence of the macroscopic contact angle $\theta$ can be gained by applying Young's equation. Because $\theta = 0$ at $P_g$ = 0, eq 1 yields

$$\gamma_{sg,P_g=0} - \gamma_{sw,P_g=0} \geq \gamma_{gw,P_g=0} \tag{8}$$

The absence of $CO_2$ accumulation at the quartz–water interface implies that $\gamma_{sw}$ is essentially invariant with $P_g$, such that eq 8 becomes

$$\gamma_{sg,P_g=0} - \gamma_{sw} \geq \gamma_{gw,P_g=0} \tag{9}$$

The combination of eqs 1 and 9 yields a relation describing the macroscopic contact angle $\theta$ at $P_g > 0$ as a function of $\gamma_{sg}$ and $\gamma_{gw}$ at $P_g = 0$ and at the pressure of interest

$$\cos\theta \geq \frac{\gamma_{sg} - \gamma_{sg,P_g=0} + \gamma_{gw,P_g=0}}{\gamma_{gw}} \tag{10}$$

If we use the symbol $\Delta$ to represent the change in interfacial energy between $P_g = 0$ and the pressure of interest, this becomes

$$\cos\theta \geq \frac{\Delta\gamma_{sg} + \gamma_{gw,P_g=0}}{\Delta\gamma_{gw} + \gamma_{gw,P_g=0}} \tag{11}$$

In short, a transition from $\theta = 0$ to $\theta > 0$ with increasing $P_g$ is possible (but not guaranteed) if the pressure-dependence of $\gamma_{sg}$ is greater than that of $\gamma_{gw}$.



https://dx.doi.org/10.1021/acs.jpcc.0c07948
J. Phys. Chem. C 2020, 124, 25382–25395

The possibility that $CO_2$ pressure has a greater impact on $\gamma_{sg}$ than on $\gamma_{gw}$ can be evaluated using the Gibbs adsorption equation (eq 6). At the $CO_2$–water interface, this relation yields

$$d\gamma_{gw} = -\Gamma_{g,gw}\, d\mu_g \tag{12}$$

where $\Gamma_{g,gw}$ is the surface excess of $CO_2$ at the curved $CO_2$–water interface. At the quartz–$CO_2$ interface, the corresponding relation must account for the adsorption of both $CO_2$ and water

$$d\gamma_{sg} = -\Gamma_{g,sg}\, d\mu_g - \Gamma_{w,sg}\, d\mu_w \tag{13}$$

If we combine eqs 12, 13 and apply $d\mu_w = -V_{m,w}\, dP_{disj}$ (from eq 3) and $\Gamma_{w,sg}V_{m,w} = h$ (from the definition of the adsorbed film thickness), we obtain

$$d\gamma_{sg} = (\Gamma_{g,sg}/\Gamma_{g,gw})d\gamma_{gw} + h\, dP_{disj} \tag{14}$$

Equation 14 shows that $P_g$ can have a greater impact on $\gamma_{sg}$ than on $\gamma_{gw}$, if either $CO_2$ adsorbs more strongly on the thin water film than on the curved $CO_2$–water interface (i.e., $\Gamma_{g,sg}/\Gamma_{g,gw} > 1$) or if $P_{disj}$ depends inversely on $P_g$. Our results on $\Gamma_{g,sg}$ and $\Gamma_{g,gw}$ (Figure 6) show that $\Gamma_{g,sg}/\Gamma_{g,gw} \leq 1$ and, hence, does not meet the first condition. The second condition, however, exists as shown by our prediction that $P_{disj}$ decreases by 16 ± 1 MPa as $P_g$ increases from 0 to 12 MPa (Figure 8). Based on our predicted film thickness ($h$ = 4.4 ± 0.7 Å), this effect would cause a decrease in $\gamma_{sg}$ by 7.0 ± 1.2 mN $m^{-1}$ as $P_g$ increases from 0 to 12 MPa, in addition to the ~35 mN $m^{-1}$ decrease expected from $CO_2$ adsorption.

**3.10. Young–Laplace Behavior Near the Three-Phase Contact Line—Impact of Interfacial Curvature on $CO_2$ Solubility in Water.** As an alternative approach to characterizing capillarity in our simulated system, we calculated the concentration of $CO_2$ dissolved in the aqueous phase and compared the results with those obtained for a flat $CO_2$–water interface (with no quartz). The application of the Kelvin equation (eq 4) to these systems indicates that the curvature of the $CO_2$ bubble should enhance $CO_2$ dissolution in water, a phenomenon observed, for example, in studies examining the Ostwald ripening of residually trapped $CO_2$ bubbles during geologic carbon sequestration.[128]

In Figure 14, we present our results on the concentration of $CO_2$ in the aqueous phase as a function of $CO_2$ pressure. Our results show that our combination of interatomic potential parameters significantly overestimates the solubility of $CO_2$ in water. This finding is consistent with previous studies indicating that the combination of the SPC/E water and EPM2 $CO_2$ models (with $CO_2$–water van der Waals interactions predicted with the Lorentz–Berthelot combining rules) approximately predicts the solubility of $CO_2$ in water[129] but underestimates the tendency of $CO_2$ to adsorb at the $CO_2$–water interface.[52,72,101] The PPL model (used here instead of the standard combining rules) predicts stronger $CO_2$–water van der Waals interactions, and hence, an improved prediction of $CO_2$ adsorption on the water surface[52] at the cost of a worse prediction of $CO_2$ solubility in the aqueous phase. Despite the offset between predicted and measured solubilities, the simulation results accurately predict the overall trend in solubility versus pressure, that is, the significant pressure-dependence of solubility below the critical pressure of $CO_2$ and the much weaker dependence at higher pressures.

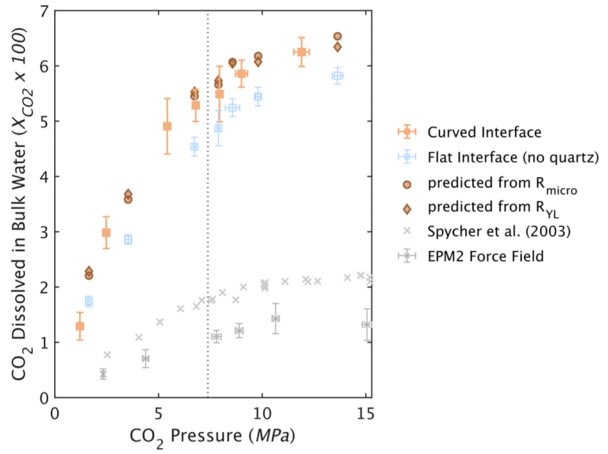


**Figure 14.** Mole fraction of $CO_2$ dissolved in the bulk water phase as a function of pressure in the bulk $CO_2$ phase. The orange and light blue symbols show MD simulation predictions in our quartz–water–$CO_2$ system (with a curved $CO_2$–water interface) and in a system with no quartz (flat $CO_2$–water interface), respectively. The brown circles and diamonds show values predicted for the quartz–water–$CO_2$ system based on the Kelvin effect using two different values for the radius of curvature of the $CO_2$–water interface: either the value directly observed ($R_{micro}$) or the value inferred from the capillary pressure using the Young–Laplace equation ($R_{YL}$). Predictions based on a compilation of experimental results are shown in gray and are more comparable to results using the SPC/E and EPM2 models with Lorentz–Berthelot combining rules.

A comparison of our simulation results obtained with flat versus curved $CO_2$–water interfaces (light blue and orange symbols in Figure 14) shows that the curvature of the fluid–fluid interface enhances $CO_2$ solubility in water by roughly 10–15%. Predictions based on the Kelvin equation (brown circles and diamonds in Figure 14) show that the magnitude of this enhancement is consistent with theory and that both measures of interfacial curvature ($R_{YL}$ and $R_{micro}$) yield equally accurate predictions of this solubility enhancement.

## 4. CONCLUSIONS

This study examines fundamental wetting and capillary properties using relatively long MD simulations of quartz–water–sc$CO_2$ systems at a range of pressures. Building upon previous studies,[12,21,44,46,55,56,58,59,62,123,125,126] this study establishes novel methodology to connect and compare continuum and nanoscale phenomena using MD simulations and gives a new perspective on wettability alterations near critical pressures. This work demonstrates that the nanoscale fluid–fluid curvature can be influenced by solid surfaces up to at least 2 nm away such that the applied continuum-scale relations must take the disjoining pressure and adsorption of thin wetting films into account. To the best of our knowledge, these findings have been demonstrated theoretically[35,42,44] but have rarely been explored using MD simulations. We characterize the distance from the interface, that a circular cap can be maintained using new methodology. In doing so, we demonstrate for the first time that structural observations of the $CO_2$ bubble show a constant circular curvature at all pressures up to 1 nm from the quartz surface, with convex nanobending up to 0.5 nm from the surface of the water film, and that stress distributions predict an increasing radius of curvature with increasing $CO_2$ pressure. This results in contact angle predictions that agree at subcritical pressures but diverge


https://dx.doi.org/10.1021/acs.jpcc.0c07948
J. Phys. Chem. C 2020, 124, 25382–25395

at higher pressures. These observations provide a new depth to these analyses and reflect the experimental database on the wettability of stringently cleaned quartz surfaces.[13,18,23−26,30,31,58,62,124−126]

The wetting trend with pressure is discussed in the context of the Young and Gibbs equations. Though other MD simulation studies have alluded to the possibility of wettability alteration because of $CO_2$ density changes,[61,62,130] the simulations and related calculations presented here demonstrate that this alteration can instead be attributed to the relationship between the capillary and disjoining pressures when simulations are fully equilibrated. Establishing the relationship of adsorbed water films to predicted $\theta$ values allows us to contribute to the discussion on the relationship between macro- and nanoscale manifestations of wettability using the augmented Young−Laplace equation. We note that the quartz surface used in this study may be more hydrophilic than silica surfaces, as silica tends to have a slightly lower surface silanol site density.[76,77] This may lead to different behavior, and we are likely observing more hydrophilic behavior in our extreme case of pure quartz compared to experimental data using silica.

We are able to reproduce theoretical predictions of disjoining pressure at various distances from the quartz surface, and our data displays the expected trends for fully and partially wetting behavior at subcritical and supercritical pressures respectively.[39,42,48] Further, we show that predictions based on Young's equation, the augmented Young−Laplace equation, and the Kelvin equation are all consistent with theory at the nanoscale.[41,42,131] The properties characterized in detail by this study are essential for accurate predictions of multiphase flow and residual and structural trapping of $scCO_2$ in the subsurface at the pore network scale. Although we focus on conditions relevant to GCS here, our results on mineral wettability and the relationship between different scales should be broadly relevant to many other areas of study. The fundamental behavior of fluid in porous media studied here opens up possibilities for studying difficult multiphase flow problems. The macro- and nanoscale properties observable in this system positions MD simulations as a promising method for resolving whether the adsorption of nanoscale water films to an interface and nanoscale capillary properties can be adequately explained by macroscopic models. Future work will focus on extracting further molecular insights on wettability alteration and on dynamic wetting parameters from both the thermal fluctuations at equilibrium and nonequilibrium MD simulations.

## ■ ASSOCIATED CONTENT

### Supporting Information

The Supporting Information is available free of charge at https://pubs.acs.org/doi/10.1021/acs.jpcc.0c07948.

MD simulation parameters, curvature results, methodology for obtaining the correct $CO_2$ equation of state relationship using LAMMPS, further results on the film spreading dynamics, and fluid density at the quartz surface and the stress anisotropy in the fluids (PDF)

## ■ AUTHOR INFORMATION


### Corresponding Author

**Emily Wei-Hsin Sun** − *Department of Civil and Environmental Engineering and High Meadows Environmental Institute, Princeton University, Princeton, New Jersey 08544, United States;* orcid.org/0000-0002-7742-427X; Phone: +1(609) 258-3021; Email: esun@princeton.edu

### Author

**Ian C. Bourg** − *Department of Civil and Environmental Engineering and High Meadows Environmental Institute, Princeton University, Princeton, New Jersey 08544, United States;* orcid.org/0000-0002-5265-7229

Complete contact information is available at: https://pubs.acs.org/10.1021/acs.jpcc.0c07948


### Notes

The authors declare no competing financial interest.

## ■ ACKNOWLEDGMENTS

This research was supported primarily by the U.S. Department of Energy, Office of Science, Office of Basic Energy Sciences, Geosciences Program under Award DE-SC0018419. We acknowledge the support of the Natural Sciences and Engineering Research Council of Canada (NSERC), cette recherche a été financée par le Conseil de Recherches en Sciences Naturelles et en Génie du Canada (CRSNG), PGSD2-532635-2019. MD simulations were performed using resources of the National Energy Research Scientific Computing Center (NERSC), which is supported by the U.S. Department of Energy, Office of Science, under award DE-AC02-05CH11231. The research presented here was improved by discussions with Laura Lammers and Elliot Chang at UC Berkeley and with Howard Stone and Michael Celia at Princeton.

## ■ REFERENCES


(1) Stocker, T. F.; Qin, D.; Plattner, G.-K.; Tignor, M. M. B.; Allen, S. K.; Boschung, J.; Nauels, A.; Xia, Y.; Bex, V.; Midgley, P. M. *Climate Change 2013—The Physical Science Basis*; Intergovernmental Panel on Climate Change, Ed.; Cambridge University Press: Cambridge, 2014.

(2) Carleton, T. A.; Hsiang, S. M. Social and Economic Impacts of Climate. *Science* **2016**, *353*, aad9837.

(3) Metz, B.; Davidson, O.; de Coninck, H.; Loos, M.; Meyer, L. *IPCC Special Report: Carbon Dioxide Capture and Storage*; Cambridge University Press, 2005.

(4) DePaolo, D. J.; Cole, D. R. Geochemistry of Geologic Carbon Sequestration: An Overview. *Rev. Mineral. Geochem.* **2013**, *77*, 1−14.

(5) Gibbins, J.; Chalmers, H. Carbon Capture and Storage. *Energy Policy* **2008**, *36*, 4317−4322.

(6) U.S. Department of Energy. *Carbon Capture, Utilization, and Storage: Climate Change, Economic Competitiveness, and Energy Security*, 2016.

(7) United Nations; Group of Experts on Cleaner Electricity Production from Fossil Fuels. *Revised Recommendations of the United Nations Economic Commission for Europe to the United Nations Framework Convention on Climate Change on How Carbon Capture and Storage in Cleaner Electricity Production and through Enhanced Oil Recovery Could Be Used In Reducing Greenhouse Gas Emissions*, 2014.

(8) Benson, S. M.; Cole, D. R. CO2 Sequestration in Deep Sedimentary Formations. *Elements* **2008**, *4*, 325−331.

(9) Iglauer, S.; Paluszny, A.; Pentland, C. H.; Blunt, M. J. Residual CO2 Imaged with X-Ray Micro-Tomography. *Geophys. Res. Lett.* **2011**, *38*, L21403.

(10) Li, B.; Benson, S. M. Influence of Small-Scale Heterogeneity on Upward CO2 Plume Migration in Storage Aquifers. *Adv. Water Resour.* **2015**, *83*, 389−404.

(11) Zhao, B.; MacMinn, C. W.; Juanes, R. Wettability Control on Multiphase Flow in Patterned Microfluidics. *Proc. Natl. Acad. Sci. U.S.A.* **2016**, *113*, 10251−10256.

(12) Arif, M.; Abu-Khamsin, S. A.; Iglauer, S. Wettability of Rock/$CO_2$/Brine and Rock/Oil/$CO_2$-Enriched-Brine Systems: Critical Parametric Analysis and Future Outlook. *Adv. Colloid Interface Sci.* **2019**, *268*, 91−113.
(13) Iglauer, S.; Pentland, C. H.; Busch, A. CO2 Wettability of Seal and Reservoir Rocks and the Implications for Carbon Geo-Sequestration. *Water Resour. Res.* **2015**, *51*, 729−774.
(14) Skurtveit, E.; Aker, E.; Soldal, M.; Angeli, M.; Wang, Z. Experimental Investigation of CO2 Breakthrough and Flow Mechanisms in Shale. *Pet. Geosci.* **2012**, *18*, 3−15.
(15) Hildenbrand, A.; Schlömer, S.; Krooss, B. M.; Littke, R. Gas Breakthrough Experiments on Pelitic Rocks: Comparative Study with N2, CO2 and CH4. *Geofluids* **2004**, *4*, 61−80.
(16) Saadatpoor, E.; Bryant, S. L.; Sepehrnoori, K. New Trapping Mechanism in Carbon Sequestration. *Transp. Porous Media* **2010**, *82*, 3−17.
(17) Pini, R.; Krevor, S. C. M.; Benson, S. M. Capillary Pressure and Heterogeneity for the CO2/Water System in Sandstone Rocks at Reservoir Conditions. *Adv. Water Resour.* **2012**, *38*, 48−59.
(18) Espinoza, D. N.; Santamarina, J. C. Water-CO2-Mineral Systems: Interfacial Tension, Contact Angle, and Diffusion - Implications to CO2 Geological Storage. *Water Resour. Res.* **2010**, *46*, W07537.
(19) Spiteri, E. J.; Juanes, R.; Blunt, M. J.; Orr, F. M. A New Model of Trapping and Relative Permeability Hysteresis for All Wettability Characteristics. *SPE J.* **2008**, *13*, 277−288.
(20) Bourg, I. C.; Beckingham, L. E.; DePaolo, D. J. The Nanoscale Basis of CO2 Trapping for Geologic Storage. *Environ. Sci. Technol.* **2015**, *49*, 10265−10284.
(21) Iglauer, S. CO2-Water-Rock Wettability: Variability, Influencing Factors, and Implications for CO2 Geostorage. *Acc. Chem. Res.* **2017**, *50*, 1134−1142.
(22) Bikkina, P. K. Contact Angle Measurements of CO2-Water-Quartz/Calcite Systems in the Perspective of Carbon Sequestration. *Int. J. Greenhouse Gas Control* **2011**, *5*, 1259−1271.
(23) Jung, J.-W.; Wan, J. Supercritical CO2 and Ionic Strength Effects on Wettability of Silica Surfaces: Equilibrium Contact Angle Measurements. *Energy Fuels* **2012**, *26*, 6053−6059.
(24) Farokhpoor, R.; Bjørkvik, B. J. A.; Lindeberg, E.; Torsæter, O. Wettability Behaviour of CO2 at Storage Conditions. *Int. J. Greenhouse Gas Control* **2013**, *12*, 18−25.
(25) Chiquet, P.; Broseta, D.; Thibeau, S. Wettability Alteration of Caprock Minerals by Carbon Dioxide. *Geofluids* **2007**, *7*, 112−122.
(26) Saraji, S.; Goual, L.; Piri, M.; Plancher, H. Wettability of Supercritical Carbon Dioxide/Water/Quartz Systems: Simultaneous Measurement of Contact Angle and Interfacial Tension at Reservoir Conditions. *Langmuir* **2013**, *29*, 6856−6866.
(27) Wan, J.; Kim, Y.; Tokunaga, T. K. Contact Angle Measurement Ambiguity in Supercritical CO2-Water-Mineral Systems: Mica as an Example. *Int. J. Greenhouse Gas Control* **2014**, *31*, 128−137.
(28) Akbarabadi, M.; Saraji, S.; Piri, M.; Georgi, D.; Delshad, M. Nano-Scale Experimental Investigation of in-Situ Wettability and Spontaneous Imbibition in Ultra-Tight Reservoir Rocks. *Adv. Water Resour.* **2017**, *107*, 160−179.
(29) Wang, S.; Tao, Z.; Persily, S. M.; Clarens, A. F. CO2 Adhesion on Hydrated Mineral Surfaces. *Environ. Sci. Technol.* **2013**, *47*, 11858−11865.
(30) Botto, J.; Fuchs, S. J.; Fouke, B. W.; Clarens, A. F.; Freiburg, J. T.; Berger, P. M.; Werth, C. J. Effects of Mineral Surface Properties on Supercritical CO2 Wettability in a Siliciclastic Reservoir. *Energy Fuels* **2017**, *31*, 5275−5285.
(31) Iglauer, S.; Salamah, A.; Sarmadivaleh, M.; Liu, K.; Phan, C. Contamination of Silica Surfaces: Impact on Water-CO2-Quartz and Glass Contact Angle Measurements. *Int. J. Greenhouse Gas Control* **2014**, *22*, 325−328.
(32) Mahadevan, J. Comments on the Paper Titled "Contact Angle Measurements of CO2-Water-Quartz/Calcite Systems in the Perspective of Carbon Sequestration": A Case of Contamination? *Int. J. Greenhouse Gas Control* **2012**, *7*, 261−262.
(33) Bikkina, P. K. Reply to the Comments on "Contact Angle Measurements of CO2-Water-Quartz/Calcite Systems in the Perspective of Carbon Sequestration.". *Int. J. Greenhouse Gas Control* **2012**, *7*, 263−264.
(34) Bikkina, P.; Shaik, I. Interfacial Tension and Contact Angle Data Relevant to Carbon Sequestration. *Carbon Capture, Utilization and Sequestration*; InTech, 2018; pp 163−186.
(35) Wang, H. From Contact Line Structures to Wetting Dynamics. *Langmuir* **2019**, *35*, 10233−10245.
(36) Kuchin, I.; Starov, V. Hysteresis of Contact Angle of Sessile Droplets on Smooth Homogeneous Solid Substrates via Disjoining/Conjoining Pressure. *Langmuir* **2015**, *31*, 5345−5352.
(37) Liu, Q.; Yu, J.; Wang, H. The Role of the Substrate Roughness in Contact Angle Hysteresis and Dynamic Deviation. *Int. J. Heat Mass Transfer* **2020**, *148*, 118985.
(38) Meakin, P.; Tartakovsky, A. M. Modeling and Simulation of Pore-Scale Multiphase Fluid Flow and Reactive Transport in Fractured and Porous Media. *Rev. Geophys.* **2009**, *47*, RG3002.
(39) Chen, L.; Yu, J.; Wang, H. Convex Nanobending at a Moving Contact Line: The Missing Mesoscopic Link in Dynamic Wetting. *ACS Nano* **2014**, *8*, 11493−11498.
(40) Rubasinghege, G.; Grassian, V. H. Role(s) of Adsorbed Water in the Surface Chemistry of Environmental Interfaces. *Chem. Commun.* **2013**, *49*, 3071−3094.
(41) Pashley, R. M. Multilayer Adsorption of Water on Silica: An Analysis of Experimental Results. *J. Colloid Interface Sci.* **1980**, *78*, 246−248.
(42) Yeh, E. K.; Newman, J.; Radke, C. J. Equilibrium Configurations of Liquid Droplets on Solid Surfaces under the Influence of Thin-Film Forces: Part I. Thermodynamics. *Colloids Surf., A* **1999**, *156*, 137−144.
(43) Wang, S.; Edwards, I. M.; Clarens, A. F. Wettability Phenomena at the CO2-Brine-Mineral Interface: Implications for Geologic Carbon Sequestration. *Environ. Sci. Technol.* **2013**, *47*, 234−241.
(44) Alizadeh Pahlavan, A.; Cueto-Felgueroso, L.; McKinley, G. H.; Juanes, R. Thin Films in Partial Wetting: Internal Selection of Contact-Line Dynamics. *Phys. Rev. Lett.* **2015**, *115*, 034502.
(45) Abu-Al-Saud, M. O.; Esmaeilzadeh, S.; Riaz, A.; Tchelepi, H. A. Pore-Scale Study of Water Salinity Effect on Thin-Film Stability for a Moving Oil Droplet. *J. Colloid Interface Sci.* **2020**, *569*, 366−377.
(46) Rücker, M.; Bartels, W.-B.; Garfi, G.; Shams, M.; Bultreys, T.; Boone, M.; Pieterse, S.; Maitland, G. C.; Krevor, S.; Cnudde, V.; Mahani, H.; Berg, S.; Georgiadis, A.; Luckham, P. F. Relationship between Wetting and Capillary Pressure in a Crude Oil/Brine/Rock System: From Nano-Scale to Core-Scale. *J. Colloid Interface Sci.* **2020**, *562*, 159−169.
(47) Abu-Al-Saud, M. O.; Riaz, A.; Tchelepi, H. A. Multiscale Level-Set Method for Accurate Modeling of Immiscible Two-Phase Flow with Deposited Thin Films on Solid Surfaces. *J. Comput. Phys.* **2017**, *333*, 297−320.
(48) De Gennes, P. G.; Hua, X.; Levinson, P. Dynamics of Wetting: Local Contact Angles. *J. Fluid Mech.* **1990**, *212*, 55−63.
(49) Leroch, S.; Wendland, M. Simulation of Forces between Humid Amorphous Silica Surfaces: A Comparison of Empirical Atomistic Force Fields. *J. Phys. Chem. C* **2012**, *116*, 26247−26261.
(50) Wensink, E. J. W.; Hoffmann, A. C.; Apol, M. E. F.; Berendsen, H. J. C. Properties of Adsorbed Water Layers and the Effect of Adsorbed Layers on Interparticle Forces by Liquid Bridging. *Langmuir* **2000**, *16*, 7392−7400.
(51) Rotenberg, B.; Patel, A. J.; Chandler, D. Molecular Explanation for Why Talc Surfaces Can Be Both Hydrophilic and Hydrophobic. *J. Am. Chem. Soc.* **2011**, *133*, 20521−20527.
(52) Nielsen, L. C.; Bourg, I. C.; Sposito, G. Predicting CO2-Water Interfacial Tension under Pressure and Temperature Conditions of Geologic CO2 Storage. *Geochim. Cosmochim. Acta* **2012**, *81*, 28−38.
(53) Hamm, L. M.; Bourg, I. C.; Wallace, A. F.; Rotenberg, B. Molecular Simulation of CO2- and CO3-Brine-Mineral Systems. *Rev. Mineral. Geochem.* **2013**, *77*, 189−228.


https://dx.doi.org/10.1021/acs.jpcc.0c07948
J. Phys. Chem. C 2020, 124, 25382−25395

(54) Kerisit, S.; Weare, J. H.; Felmy, A. R. Structure and Dynamics of Forsterite-ScCO2/H2O Interfaces as a Function of Water Content. *Geochim. Cosmochim. Acta* **2012**, *84*, 137−151.
(55) Tenney, C. M.; Cygan, R. T. Molecular Simulation of Carbon Dioxide, Brine, and Clay Mineral Interactions and Determination of Contact Angles. *Environ. Sci. Technol.* **2014**, *48*, 2035−2042.
(56) Silvestri, A.; Ataman, E.; Budi, A.; Stipp, S. L. S.; Gale, J. D.; Raiteri, P. Wetting Properties of the CO2-Water-Calcite System via Molecular Simulations: Shape and Size Effects. *Langmuir* **2019**, *35*, 16669−16678.
(57) Bagherzadeh, S. A.; Englezos, P.; Alavi, S.; Ripmeester, J. A. Influence of Hydrated Silica Surfaces on Interfacial Water in the Presence of Clathrate Hydrate Forming Gases. *J. Phys. Chem. C* **2012**, *116*, 24907−24915.
(58) Liang, Y.; Tsuji, S.; Jia, J.; Tsuji, T.; Matsuoka, T. Modeling CO2−Water−Mineral Wettability and Mineralization for Carbon Geosequestration. *Acc. Chem. Res.* **2017**, *50*, 1530−1540.
(59) Chen, C.; Zhang, N.; Li, W.; Song, Y. Water Contact Angle Dependence with Hydroxyl Functional Groups on Silica Surfaces under CO2 Sequestration Conditions. *Environ. Sci. Technol.* **2015**, *49*, 14680−14687.
(60) Chen, C.; Dong, B.; Zhang, N.; Li, W.; Song, Y. Pressure and Temperature Dependence of Contact Angles for CO2/Water/Silica Systems Predicted by Molecular Dynamics Simulations. *Energy Fuels* **2016**, *30*, 5027−5034.
(61) Iglauer, S.; Mathew, M. S.; Bresme, F. Molecular Dynamics Computations of Brine−CO2 Interfacial Tensions and Brine−CO2−Quartz Contact Angles and Their Effects on Structural and Residual Trapping Mechanisms in Carbon Geo-Sequestration. *J. Colloid Interface Sci.* **2012**, *386*, 405−414.
(62) Huang, P.; Shen, L.; Gan, Y.; Maggi, F.; El-Zein, A.; Pan, Z. Atomistic Study of Dynamic Contact Angles in CO2−Water−Silica System. *Langmuir* **2019**, *35*, 5324−5332.
(63) Abramov, A.; Iglauer, S. Analysis of Individual Molecular Dynamics Snapshots Simulating Wetting of Surfaces Using Spheroidal Geometric Constructions. *J. Chem. Phys.* **2019**, *151*, 064705.
(64) Tuller, M.; Or, D.; Dudley, L. M. Adsorption and Capillary Condensation in Porous Media: Liquid Retention and Interfacial Configurations in Angular Pores. *Water Resour. Res.* **1999**, *35*, 1949−1964.
(65) Tang, M.; Cziczo, D. J.; Grassian, V. H. Interactions of Water with Mineral Dust Aerosol: Water Adsorption, Hygroscopicity, Cloud Condensation, and Ice Nucleation. *Chem. Rev.* **2016**, *116*, 4205−4259.
(66) Yao, X.; Song, Y.; Jiang, L. Applications of Bio-Inspired Special Wettable Surfaces. *Adv. Mater.* **2011**, *23*, 719−734.
(67) Boo, C.; Hong, S.; Elimelech, M. Relating Organic Fouling in Membrane Distillation to Intermolecular Adhesion Forces and Interfacial Surface Energies. *Environ. Sci. Technol.* **2018**, *52*, 14198−14207.
(68) Mugele, F.; Baret, J.-C. Electrowetting: From Basics to Applications. *J. Phys.: Condens. Matter* **2005**, *17*, R705−R774.
(69) Wang, Z.; Elimelech, M.; Lin, S. Environmental Applications of Interfacial Materials with Special Wettability. *Environ. Sci. Technol.* **2016**, *50*, 2132−2150.
(70) Plimpton, S. Fast Parallel Algorithms for Short-Range Molecular Dynamics. *J. Comput. Phys.* **1995**, *117*, 1−19.
(71) Amirfazli, A.; Neumann, A. W. Status of the Three-Phase Line Tension: A Review. *Adv. Colloid Interface Sci.* **2004**, *110*, 121−141.
(72) Kvamme, B.; Kuznetsova, T.; Hebach, A.; Oberhof, A.; Lunde, E. Measurements and Modelling of Interfacial Tension for Water +carbon Dioxide Systems at Elevated Pressures. *Comput. Mater. Sci.* **2007**, *38*, 506−513.
(73) Kihara, K. An X-ray Study of the Temperature Dependence of the Quartz Structure. *Eur. J. Mineral.* **1990**, *2*, 63−78.
(74) Schlegel, M. L.; Nagy, K. L.; Fenter, P.; Sturchio, N. C. Structures of Quartz (1010)- and (1011)-Water Interfaces Determined by x-Ray Reflectivity and Atomic Force Microscopy of Natural Growth Surfaces. *Geochim. Cosmochim. Acta* **2002**, *66*, 3037−3054.
(75) Du, Z.; De Leeuw, N. H. A Combined Density Functional Theory and Interatomic Potential-Based Simulation Study of the Hydration of Nano-Particulate Silicate Surfaces. *Surf. Sci.* **2004**, *554*, 193−210.
(76) Zhuravlev, L. T. The Surface Chemistry of Amorphous Silica. Zhuravlev Model. *Colloids Surf., A* **2000**, *173*, 1−38.
(77) Lorenz, C. D.; Crozier, P. S.; Anderson, J. A.; Travesset, A. Molecular Dynamics of Ionic Transport and Electrokinetic Effects in Realistic Silica Channels. *J. Phys. Chem. C* **2008**, *112*, 10222−10232.
(78) Cruz-Chu, E. R.; Aksimentiev, A.; Schulten, K. Water−Silica Force Field for Simulating Nanodevices. *J. Phys. Chem. B* **2006**, *110*, 21497−21508.
(79) Wang, X.; Jameson, C. J.; Murad, S. Modeling Enantiomeric Separations as an Interfacial Process Using Amylose Tris(3,5-Dimethylphenyl Carbamate) (ADMPC) Polymers Coated on Amorphous Silica. *Langmuir* **2020**, *36*, 1113−1124.
(80) Cygan, R. T.; Liang, J.-J.; Kalinichev, A. G. Molecular Models of Hydroxide, Oxyhydroxide, and Clay Phases and the Development of a General Force Field. *J. Phys. Chem. B* **2004**, *108*, 1255−1266.
(81) Berendsen, H. J. C.; Grigera, J. R.; Straatsma, T. P. The Missing Term in Effective Pair Potentials. *J. Phys. Chem.* **1987**, *91*, 6269−6271.
(82) Harris, J. G.; Yung, K. H. Carbon Dioxide's Liquid-Vapor Coexistence Curve And Critical Properties as Predicted by a Simple Molecular Model. *J. Phys. Chem.* **1995**, *99*, 12021−12024.
(83) In Het Panhuis, M.; Patterson, C. H.; Lynden-Bell, R. M. A Molecular Dynamics Study of Carbon Dioxide in Water: Diffusion, Structure and Thermodynamics. *Mol. Phys.* **1998**, *94*, 963−972.
(84) Hura, G.; Russo, D.; Glaeser, R. M.; Head-Gordon, T.; Krack, M.; Parrinello, M. Water Structure as a Function of Temperature from X-Ray Scattering Experiments and Ab Initio Molecular Dynamics. *Phys. Chem. Chem. Phys.* **2003**, *5*, 1981−1991.
(85) Alejandre, J.; Tildesley, D. J.; Chapela, G. A. Molecular Dynamics Simulation of the Orthobaric Densities and Surface Tension of Water. *J. Chem. Phys.* **1995**, *102*, 4574−4583.
(86) Duan, Z.; Zhang, Z. Equation of State of the H2O, CO2, and H2O−CO2 Systems up to 10 GPa and 2573.15 K: Molecular Dynamics Simulations with Ab Initio Potential Surface. *Geochim. Cosmochim. Acta* **2006**, *70*, 2311−2324.
(87) Bourg, I. C.; Steefel, C. I. Molecular Dynamics Simulations of Water Structure and Diffusion in Silica Nanopores. *J. Phys. Chem. C* **2012**, *116*, 11556−11564.
(88) Skelton, A. A.; Wesolowski, D. J.; Cummings, P. T. Investigating the Quartz $(10\bar{1}0)$/Water Interface Using Classical and Ab Initio Molecular Dynamics. *Langmuir* **2011**, *27*, 8700−8709.
(89) Marry, V.; Dubois, E.; Malikova, N.; Durand-Vidal, S.; Longeville, S.; Breu, J. Water Dynamics in Hectorite Clays: Influence of Temperature Studied by Coupling Neutron Spin Echo and Molecular Dynamics. *Environ. Sci. Technol.* **2011**, *45*, 2850−2855.
(90) da Rocha, S. R. P.; Johnston, K. P.; Westacott, R. E.; Rossky, P. J. Molecular Structure of the Water−Supercritical CO2 Interface. *J. Phys. Chem. B* **2001**, *105*, 12092−12104.
(91) Vorholz, J.; Harismiadis, V. I.; Rumpf, B.; Panagiotopoulos, A. Z.; Maurer, G. Vapor+liquid Equilibrium of Water, Carbon Dioxide, and the Binary System, Water+carbon Dioxide, from Molecular Simulation. *Fluid Phase Equilib.* **2000**, *170*, 203−234.
(92) Vega, C.; de Miguel, E. Surface Tension of the Most Popular Models of Water by Using the Test-Area Simulation Method. *J. Chem. Phys.* **2007**, *126*, 154707.
(93) Ryckaert, J.-P.; Ciccotti, G.; Berendsen, H. J. C. Numerical Integration of the Cartesian Equations of Motion of a System with Constraints: Molecular Dynamics of n-Alkanes. *J. Comput. Phys.* **1977**, *23*, 327−341.
(94) Yu, K.; McDaniel, J. G.; Schmidt, J. R. Physically Motivated, Robust, Ab Initio Force Fields for CO2 and N2. *J. Phys. Chem. B* **2011**, *115*, 10054−10063.
(95) Hockney, R. W.; Eastwood, J. W. Particle-Particle-Particle-Mesh (P3M) Algorithms. *Computer Simulation Using Particles*; Taylor & Francis Group: New York, 1988; pp 267−304.


https://dx.doi.org/10.1021/acs.jpcc.0c07948
J. Phys. Chem. C 2020, 124, 25382−25395

(96) Anagnostopoulos, A.; Navarro, H.; Alexiadis, A.; Ding, Y. Wettability of NaNO3 and KNO3 on MgO and Carbon Surfaces—Understanding the Substrate and the Length Scale Effects. *J. Phys. Chem. C* **2020**, *124*, 8140−8152.
(97) Bourg, I. C.; Sposito, G. Molecular Dynamics Simulations of the Electrical Double Layer on Smectite Surfaces Contacting Concentrated Mixed Electrolyte (NaCl-CaCl2) Solutions. *J. Colloid Interface Sci.* **2011**, *360*, 701−715.
(98) Schrader, A. M.; Monroe, J. I.; Sheil, R.; Dobbs, H. A.; Keller, T. J.; Li, Y.; Jain, S.; Shell, M. S.; Israelachvili, J. N.; Han, S. Surface Chemical Heterogeneity Modulates Silica Surface Hydration. *Proc. Natl. Acad. Sci. U.S.A.* **2018**, *115*, 2890−2895.
(99) Schmatz, J.; Urai, J. L.; Berg, S.; Ott, H. Nanoscale Imaging of Pore-Scale Fluid-Fluid-Solid Contacts in Sandstone. *Geophys. Res. Lett.* **2015**, *42*, 2189−2195.
(100) Lehmkühler, F.; Paulus, M.; Sternemann, C.; Lietz, D.; Venturini, F.; Gutt, C.; Tolan, M. The Carbon Dioxide−Water Interface at Conditions of Gas Hydrate Formation. *J. Am. Chem. Soc.* **2009**, *131*, 585−589.
(101) Zhang, H.; Singer, S. J. Analysis of the Subcritical Carbon Dioxide−Water Interface. *J. Phys. Chem. A* **2011**, *115*, 6285−6296.
(102) Biscay, F.; Ghoufi, A.; Lachet, V.; Malfreyt, P. Monte Carlo Simulations of the Pressure Dependence of the Water−Acid Gas Interfacial Tensions. *J. Phys. Chem. B* **2009**, *113*, 14277−14290.
(103) Rother, G.; Krukowski, E. G.; Wallacher, D.; Grimm, N.; Bodnar, R. J.; Cole, D. R. Pore Size Effects on the Sorption of Supercritical CO2 in Mesoporous CPG-10 Silica. *J. Phys. Chem. C* **2012**, *116*, 917−922.
(104) Rother, G.; Melnichenko, Y. B.; Cole, D. R.; Frielinghaus, H.; Wignall, G. D. Microstructural Characterization of Adsorption and Depletion Regimes of Supercritical Fluids in Nanopores. *J. Phys. Chem. C* **2007**, *111*, 15736−15742.
(105) Chiquet, P.; Daridon, J.-L.; Broseta, D.; Thibeau, S. CO2/Water Interfacial Tensions under Pressure and Temperature Conditions of CO2 Geological Storage. *Energy Convers. Manage.* **2007**, *48*, 736−744.
(106) Khalkhali, M.; Kazemi, N.; Zhang, H.; Liu, Q. Wetting at the Nanoscale: A Molecular Dynamics Study. *J. Chem. Phys.* **2017**, *146*, 114704.
(107) Fernández-Toledano, J.-C.; Blake, T. D.; De Coninck, J. Contact-Line Fluctuations and Dynamic Wetting. *J. Colloid Interface Sci.* **2019**, *540*, 322−329.
(108) Taubin, G. Estimation of Planar Curves, Surfaces, and Nonplanar Space Curves Defined by Implicit Equations with Applications to Edge and Range Image Segmentation. *IEEE Trans. Pattern Anal. Mach. Intell.* **1991**, *13*, 1115−1138.
(109) Chernov, N. Circle Fit (Taubin method). https://www.mathworks.com/matlabcentral/fileexchange/22678-circle-fit-taubin-method (accessed May 30, 2020).
(110) Lemmon, E. W.; McLinden, M. O.; Friend, D. G. Thermophysical Properties of Fluid Systems. In *NIST Chemistry WebBook, NIST Standard Reference Database Number 69*; Linstrom, P. J., Mallard, W. G., Eds.; National Institute of Standards and Technology: Gaithersburg MD, 20899, 2018.
(111) Derjaguin, B. V.; Churaev, N. V.; Muller, V. M. The Thermodynamic Theory of Stability of Thin Films. *Surface Forces*; Springer US: Boston, MA, 1987; pp 53−83.
(112) Kim, T. W.; Tokunaga, T. K.; Shuman, D. B.; Sutton, S. R.; Newville, M.; Lanzirotti, A. Thickness Measurements of Nanoscale Brine Films on Silica Surfaces under Geologic $CO_2$ Sequestration Conditions Using Synchrotron X-Ray Fluorescence. *Water Resour. Res.* **2012**, *48*, W09558.
(113) Loring, J. S.; Thompson, C. J.; Wang, Z.; Joly, A. G.; Sklarew, D. S.; Schaef, H. T.; Ilton, E. S.; Rosso, K. M.; Felmy, A. R. In Situ Infrared Spectroscopic Study of Forsterite Carbonation in Wet Supercritical CO2. *Environ. Sci. Technol.* **2011**, *45*, 6204−6210.
(114) Clarke, D. R.; Gee, M. L. Wetting of Surfaces and Grain Boundaries. In *Materials Interfaces (UK)*; Wolf, D., Yip, S., Eds.; Chapman & Hall: London, 1992; pp 255−272.
(115) Asay, D. B.; Barnette, A. L.; Kim, S. H. Effects of Surface Chemistry on Structure and Thermodynamics of Water Layers at Solid−Vapor Interfaces. *J. Phys. Chem. C* **2009**, *113*, 2128−2133.
(116) Tokunaga, T. K. Reply to Comment by Philippe Baveye on "Physicochemical Controls on Adsorbed Water Film Thickness in Unsaturated Geological Media". *Water Resour. Res.* **2012**, *48*, W11803.
(117) Beaglehole, D.; Christenson, H. K. Vapor Adsorption on Mica and Silicon: Entropy Effects, Layering, and Surface Forces. *J. Phys. Chem.* **1992**, *96*, 3395−3403.
(118) Tokunaga, T. K. Physicochemical Controls on Adsorbed Water Film Thickness in Unsaturated Geological Media. *Water Resour. Res.* **2011**, *47*, W08514.
(119) Derjaguin, B. V. Some Results from 50 Years' Research on Surface Forces. *Prog. Surf. Sci.* **1992**, *40*, 240−251.
(120) Irving, J. H.; Kirkwood, J. G. The Statistical Mechanical Theory of Transport Processes. IV. The Equations of Hydrodynamics. *J. Chem. Phys.* **1950**, *18*, 817−829.
(121) Vargaftik, N. B.; Volkov, B. N.; Voljak, L. D. International Tables of the Surface Tension of Water. *J. Phys. Chem. Ref. Data* **1983**, *12*, 817−820.
(122) Butt, H.-J.; Graf, K.; Kappl, M. *Physics and Chemistry of Interfaces*, 3rd ed.; John Wiley & Sons: Weinheim, 2013.
(123) Jiang, H.; Müller-Plathe, F.; Panagiotopoulos, A. Z. Contact Angles from Young's Equation in Molecular Dynamics Simulations. *J. Chem. Phys.* **2017**, *147*, 084708.
(124) Al-Yaseri, A. Z.; Roshan, H.; Lebedev, M.; Barifcani, A.; Iglauer, S. Dependence of Quartz Wettability on Fluid Density. *Geophys. Res. Lett.* **2016**, *43*, 3771−3776.
(125) Arif, M.; Al-Yaseri, A. Z.; Barifcani, A.; Lebedev, M.; Iglauer, S. Impact of Pressure and Temperature on CO2−Brine−Mica Contact Angles and CO2−Brine Interfacial Tension: Implications for Carbon Geo-Sequestration. *J. Colloid Interface Sci.* **2016**, *462*, 208−215.
(126) Sarmadivaleh, M.; Al-Yaseri, A. Z.; Iglauer, S. Influence of Temperature and Pressure on Quartz−Water−CO2 Contact Angle and CO2−Water Interfacial Tension. *J. Colloid Interface Sci.* **2015**, *441*, 59−64.
(127) Deng, Y.; Chen, L.; Yu, J.; Wang, H. Nanoscopic Morphology of Equilibrium Thin Water Film near the Contact Line. *Int. J. Heat Mass Transfer* **2015**, *91*, 1114−1118.
(128) de Chalendar, J. A.; Garing, C.; Benson, S. M. Pore-Scale Modelling of Ostwald Ripening. *J. Fluid Mech.* **2018**, *835*, 363−392.
(129) Gadikota, G.; Dazas, B.; Rother, G.; Cheshire, M. C.; Bourg, I. C. Hydrophobic Solvation of Gases (CO2, CH4, H2, Noble Gases) in Clay Interlayer Nanopores. *J. Phys. Chem. C* **2017**, *121*, 26539−26550.
(130) Dickson, J. L.; Gupta, G.; Horozov, T. S.; Binks, B. P.; Johnston, K. P. Wetting Phenomena at the CO2/Water/Glass Interface. *Langmuir* **2006**, *22*, 2161−2170.
(131) Spycher, N.; Pruess, K.; Ennis-King, J. CO2-H2O Mixtures in the Geological Sequestration of CO2. I. Assessment and Calculation of Mutual Solubilities from 12 to 100°C and up to 600 Bar. *Geochim. Cosmochim. Acta* **2003**, *67*, 3015−3031.


https://dx.doi.org/10.1021/acs.jpcc.0c07948
J. Phys. Chem. C 2020, 124, 25382−25395